J Mater Sci: Mater Electron
DOI 10.1007/s10854-017-7605-z

One-step synthesis of $CaMoO_4$: Eu^{3+} nanospheres by ultrasonic spray pyrolysis

C. R. R. Almeida[1] · L. X. Lovisa[1] · A. A. G. Santiago[1] · M. S. Li[2] · E. Longo[3] · C. A. Paskocimas[1] · F. V. Motta[1] · M. R. D. Bomio[1]

Received: 7 March 2017 / Accepted: 25 July 2017

Abstract In this paper, $CaMoO_4$ and of Eu^{3+}-doped $CaMoO_4$ nanospheres were prepared by a spray pyrolysis method and characterized by X-ray diffraction (XRD), field emission scanning electron microscopy (FESEM), Raman spectra and photoluminescence spectroscopy. XRD patterns indicate that these crystals have a scheelite-type tetragonal structure. The morphology of the $CaMoO_4$: Eu^{3+} nanospheres was investigated from the FESEM results and it was observed the formation of spherical particles peculiar to the synthesis method used. Sample of pure $CaMoO_4$ thermally treated 1000 °C exhibit a photoluminescence behavior broadband type with emission in white light according to the calculated values of the CIE coordinates: x = 0.37, y = 0.37. The emission intensity in the red for samples doped with Eu^{3+} ($^5D_0 \rightarrow {}^7F_2$ in 615 nm) increases directly with the dopant concentration.

1 Introduction

Alkaline earth metal molybdates $MMoO_4$ (M = Ca, Sr, and Ba) are important materials due to remarkable luminescent behavior and structural properties with various practical applications in different fields that involve chemical and biological applications, sensor and detector, display devices, light emitting diodes (LEDs), optical fibers, scintillator materials, catalysis and lithium ion batteries [1–3]. Among these compounds, calcium molybdate, $CaMoO_4$, is one of the most attractive members of this family due to its very interesting physical and chemical properties as well as electronic structure, their high luminescence intensity, good thermal and chemical stability and high density. These properties allow it to be a good host material for luminescent materials under ultraviolet (UV) and X-ray excitation [2, 4–15].

$CaMoO_4$ presents a body-centered scheelite structure, which belongs to the tetragonal $I4_1/a$ space group and contains two formula units per primitive cell. In this crystal, the building blocks of this structure are the (MoO_4) and (CaO_8) clusters corresponding to the local coordination in which Mo cation is linked to four equivalent O anions to construct (MoO_4) tetrahedral clusters while the Ca cation forms (CaO_8) octahedral clusters and it shares corners with eight adjacent O anions in (MoO_4) tetrahedrons. In turn, (CaO_8) octahedral connect via its edges and form a 3D framework [16, 17]. In particular, the optical behavior of $CaMoO_4$ is associated to the stability and luminescent properties of (MoO_4) tetrahedron cluster with strong absorption in the UV region due to the charge transfer from oxygen to metal.

A plethora of synthetic routes was successfully used to obtain $CaMoO_4$ including the flux method. It has also been employed the Czochralski technique, floating zone-like technique, microemulsion process, citrate complex method, co-precipitation method, electrospinning process, chemical deposition, hydrothermal/solvo thermal routines, and microwave assisted techniques [7, 13, 18–31].

✉ L. X. Lovisa
lauraengmat@hotmail.com

✉ M. R. D. Bomio
mauricio.bomio@ct.ufrn.br

[1] LSQM—Laboratório de Síntese Química de Materiais, DEMAT, UFRN, Natal, Campus, Lagoa Nova, Natal, RN CEP 59078-900, Brazil

[2] IFSC, USP, Av. Trabalhador São Carlense, 400, São Carlos, SP CEP 13566-590, Brazil

[3] LIEC—Laboratório interdisciplinar de eletroquímica e cerâmica de DQ, UFSCar, São Carlos, SP CEP 13565-905, Brazil

Published online: 02 August 2017

The solid state chemical routes involve preparations that are often complicated to obtain the correct stoichiometry and still require post-calcination to obtain high crystallinity [32]. Chemical routes via liquid phase are processes that employ a large amount of solvents. Among these, the use of surfactants contaminates the particles produced in most of the more advanced processes. Gas-phase routes (for example those which form aerosols), on the other hand, offer high purity. In addition, the techniques that use aerosols reduce the generation of waste, which makes them more attractive for large-scale production. The simplicity of the spray-pyrolysis method in manipulating and depositing nanoparticles in suspension, aiming to form specific structures, makes the science and technology of aerosols are one of the enabled areas of great performance in nanotechnology [33]. This method consists of only a single step, presents excellent reproducibility and is capable of obtaining particles with controlled properties for special applications in various industrial segments. Control of the size and morphology of the particles produced are mainly determined by the type of aerosol generator [34]. Consequently, atomization is the point of great importance of our work. The ultrasonic atomization, used in our experimental procedure, generates droplets with a fairly uniform size distribution [35].

$CaMoO_4$ shows a broad blue/green, blue–green luminescence emission peak in the range 350–650 nm with a peak maximum around 500 nm. This peak maximum, however, varies with the particle size and oxygen vacancies in the lattice [9]. It is related to the electron–hole recombination after excitation through the band gap of the charge transfer (CT) from O to Mo ($2p \rightarrow 4d$ orbital) in the (MoO_4) tetrahedron cluster itself [10]. Since the emission band is very broad, it is difficult to tune its color, particularly for lighting and display applications. On the other hand, $CaMoO_4$ is a good host material and its luminescence properties can be altered by doping with rare-earth ions and the energy transfer process from the (MoO_4) cluster to the rare-earth ions can easily occur, which can greatly enhance the external quantum efficiency of the rare-earth ions doped materials. Eu has a poor absorption cross-section due to the forbidden nature of *f–f* transitions and it shows poor luminescence emission [11]. To overcome this problem, materials with high absorption cross-section can be manipulated and Eu^{3+} was already used to enhance the luminescence or intrinsic properties of various molybdate matrices.

$CaMoO_4$ is one of the most studied ceramics as a host matrix, especially, when doped with europium (Eu^{3+}), resulting in a bright red emission [2, 36]. In particular, due to the effect of polarization of the (MoO_4) cluster, the Eu^{3+} doped $CaMoO_4$ possesses strong absorption corresponding to Eu^{3+} 4f–4f transition in the near UV and blue light region [4] and it is generally considered as a good red phosphor [37–40] resulting in a bright red emission.

In literature, different synthesis strategies have been used to improve the luminescent efficiency of the as-prepared luminescent Eu^{3+} ion-doped calcium molybdate nanocrystals (NCs). Yang et al. used polyethylene glycol (PEG), Tween-80, sodium dodecyl sulphonate (SAS) and cetyltrimethylammonium bromide (CTAB) as surfactants to prepare the $CaMoO_4$:Eu by the coprecipitation method [7]. Parchur et al. prepared the $CaMoO_4$:Eu nanoparticles using urea hydrolysis in ethylene glycol at low temperature and investigated effect of their concentration and temperature on luminescent properties [4, 36]. Very recently, two groups reported a similar synthesis strategy to prepare the $CaMoO_4$: Eu nanoparticles. In this preparation method they grow $CaMoO_4$:Ln nanoparticles by the flux growth method using Na_2MoO_4 as a solvent at a temperature range of 600–1350 °C and investigated the luminescent properties at different temperature and pressure under different experimental conditions [5, 41]. In Raju et al.'s report, spherulite morphology $CaMoO_4$:Eu nanoparticles were synthesized by the hydrothermal process and it was investigated the influence of crystallinity and temperature on luminescent properties of the as-prepared nanomaterials [2].

The main goal of this article is to investigate the synthesis of both $CaMoO_4$ and Eu^{3+}-doped $CaMoO_4$ nanoparticles by means of the spray pyrolysis method. This approach is simple and environmentally friendly. The as-synthesized samples were characterized by X-ray diffraction and Rietveld refinement, Raman spectroscopy and field emission scanning electron microscopy techniques.

The rest of the paper is divided into two sections. Next, we present the experimental details including the synthesis and characterization. Our results are discussed in three separate subsections: X-ray diffraction measurements, band structure, FE-SEM analyses and photoluminescence of the $CaMoO_4$ and Eu^{3+}-doped $CaMoO_4$ nanoparticles. Main conclusions are summarized in the last section.

2 Experimental

2.1 Materials

Acid Molybdic (H_2MoO_4), (Alfa Aesar), calcium nitrate ($Ca(NO_3)_2{\cdot}4H_2O$) (Alfa Aesar), europium nitrate (Alfa Aesar) and distilled water were used as received to prepare the $CaMoO_4$:Eu nanocrystals.

2.2 Preparation of CaMoO4:Eu nanocrystals (CMO:xEu)

The CMO:xEu NCs were obtained by the ultrasonic spray pyrolysis method. The precursor solution was prepared by dissolving 0.045 mol of $Ca(NO_3)_2{\cdot}4H_2O$ and 0.09 mol of H_2MoO_4 in 100 mL of distilled water. Figure 1 shows a schematic of the spray pyrolysis system. The droplet generator comprised an ultrasonic nebulizer. The laminar flow aerosol reactor used in the present study was a quartz tube of 37 mm inner diameter and 1.86 m length, which was inserted into a horizontal electric furnace. The precursor solution was atomized at a frequency of 2.4 MHz by using the ultrasonic nebulizer. The sprayed droplets were carried to the reactor, heated by an electric furnace at 1000 °C in air, and converted into solid oxide particles within the laminar flow aerosol reactor. The resulting particles were collected at the reactor exit by an electrostatic precipitator. The overall flow rate of air used as a carrier gas was 2 L min^{-1}.

The residence time of the CMO: xEu^{3+} solution in the reactor is a function of the drag gas flow and the reactor area volume according to Eq. 1 [42].

$$T = \frac{R}{60Q} \tag{1}$$

where T is the residence time (s), R is the gas flow rate (L min^{-1}) and V is the reactor volume (L). The reactor volume was 1.61 L and the air flow rate was 2 L min^{-1}. From this relation, it is stated that the mean time of synthesis is approximately 48 s.

Figure 1 presents a schematic of all the stages involved in the synthesis and growth of CMO and CMO:xEu nanocrystals processed in the reactor. First, stoichiometric quantities of the $Ca(NO_3)_2{\cdot}4H_2O$ and H_2MoO_4 precursors were separately dissolved in one tube containing 100 mL of deionized water. In this solution, the solvation energy of H_2O molecules causes fast dissociation of the reagents, i.e., the Ca^{2+} and MoO_3^{2-} ions are solvated by the H_2O and MoO_3^{2-} species (solution A) and (solution B = solution A + Eu^{3+}). It is well known that the Ca atoms coordinate with four H_2O and two NO_3^{1-}, and MoO_3^{2-} atoms coordinate with two $H^+$and one H_2O to form distorted octahedral $Ca(H_2O)_4.(NO_3)_2$ and $MoO_3(H_2O)_2H$ clusters. The partial negative charges of these cluster complexes are electrostatically attracted by the Ca clusters, while the positive charges of the Ca clusters attract the MoO_3^{2-} clusters. Due to the difference in the electronic density of the Ca^{2+} and MoO_3^{2-} cluster complexes, there is a strong electrostatic attraction between them. Upon evaporation of the solvent, the viscosity of water decreases and the mobility of the cluster complex is then favored, considerably increasing the effective rate of collisions between the species in the solution. Moreover, the thermal decomposition (Fig. 1—stage 1) occurs directly in the nucleation sites, forcing the crystallization kinetics of the primary crystals. As these nuclei have free rotation, collide at random, and can rearrange in relation to each other through motion, nanocrystals are effectively generated (Fig. 1—stages 2 and 3). Smaller

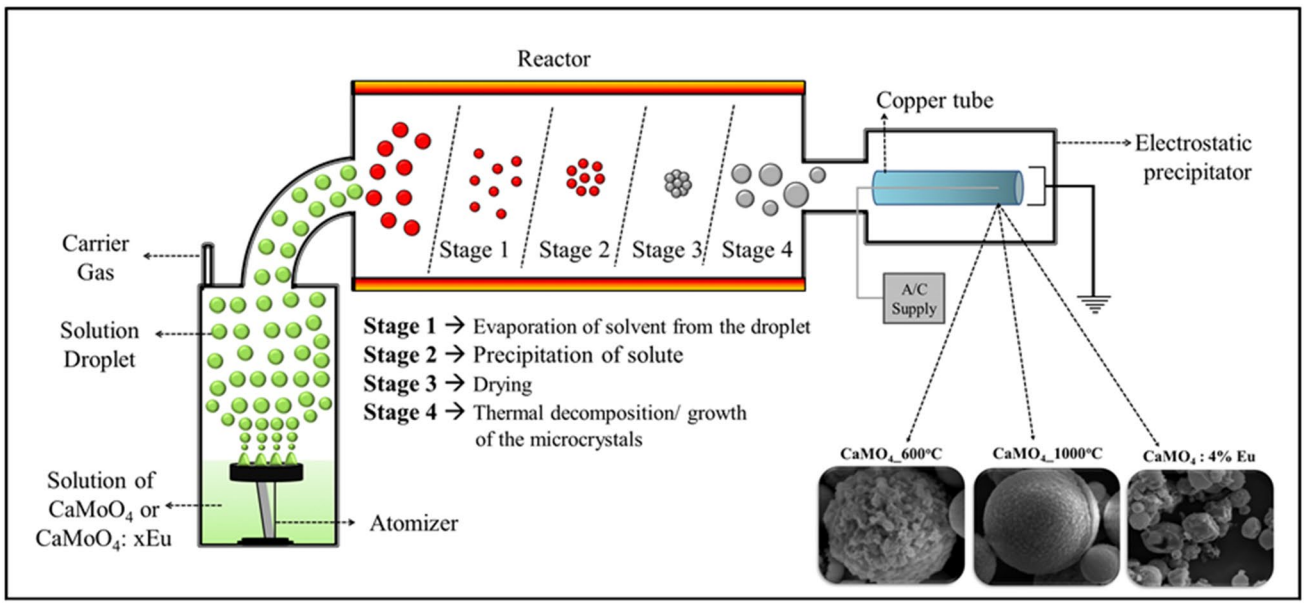

Fig. 1 Schematic diagram of the experimental apparatus and the formation of $CaMoO_4$ and $CaMoO_4$:xEu nanocrystals obtained by one-pot ultrasonic spray pyrolysis

nanocrystals tend to undergo self-assembly (Fig. 1—stage 4), possibly via Van der Waals [27] interactions in order to achieve the minimum energy per volume ratio [28]. Besides favoring the growth kinetics of the nanocrystals, thermal decomposition may favor heterogeneous nucleation and aggregation of the CMO (solution A) and CMO:xEu (Solution B) nanocrystals. Figure 1—stage 5 shows the proposed growth mechanism responsible for the formation and growth of the aggregated CMO or CMO:xEu nanocrystals. The high drying temperature can produce incremental temperature differences between the outer surface of the wet nanoparticles and the wet core, which in turn, will lead to thermal stress in the crystals.

2.3 Characterization of CMO:xEu nanocrystals

The CMO:xEu NCs were structurally characterized by XRD using a Shimadzu XRD 7000 instrument with Cu-Kα radiation (λ = 1.5406 Å) in the 2θ range from 10 to 80° at a scanning rate of 0.02° s^{-1}. Micro Raman spectroscopy measurements were recorded using a T-64000 spectrometer (Jobin-Yvon, France) triple monochromator coupled to a CCD detector. The spectra were performed using a 514.5 nm wavelength of an argon ion laser, keeping its maximum output power at 8 mW. The morphologies were investigated using field-emission gun scanning electron microscopy (FEG-SEM; Carl Zeiss, Supra 35-VP Model, Germany) operated at 6 kV. The UV–Vis diffuse reflectance spectrum was measured at room temperature using a UV–Vis spectrometer. The Photoluminescence (PL) spectra were acquired with an Ash Monospec 27 monochromator (Thermal Jarrel, USA) and a R4446 photomultiplier (Hamamatsu Photonics, USA). The 350 nm beam of a krypton ion laser (Coherent Innova 90 K) was used as the excitation source while its maximum output power was kept at 200 mW. All measurements were performed at room temperature.

3 Results

The XRD pattern presented in Fig. 2a, b shows the diffraction peaks characteristics of CMO and CMO:xEu, respectively. They can be indexed in a scheelite tetragonal unit cell with space group $I4_1/a$ in C_{4h}^6 symmetry (JCPDS-41-1431). The XRD patterns of the samples (Fig. 2b) showed

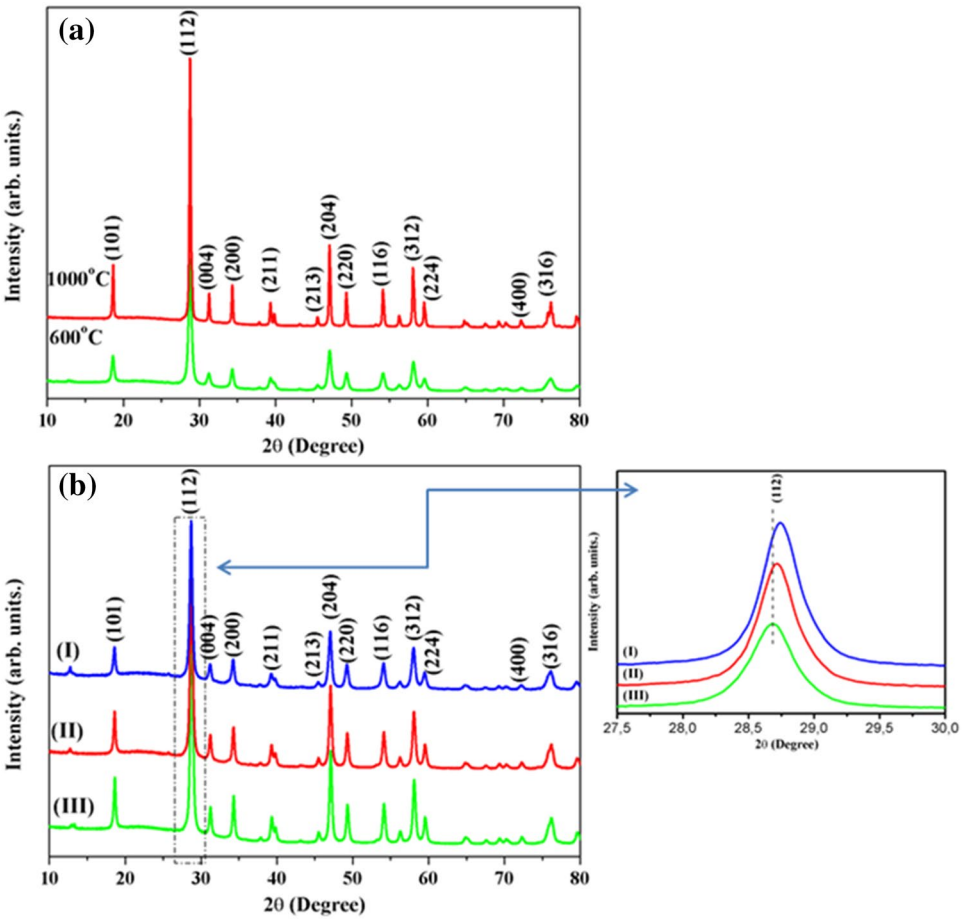

Fig. 2 XRD patterns **a** CMO and **b** CMO:xEu (*I*) x: 1, (*II*) x: 2 and (*III*) x: 4 mol % obtained by one-pot ultrasonic spray pyrolysis

that the CMO:xEu NCs are structurally related to the scheelite tetragonal crystalline phase. Due to the size of the ionic radii of Ca^{2+} (r = 1.12 Å) and Eu^{3+} (r = 1.07 Å) are near one another and the replacement of Eu^{3+} sites on the Ca^{2+} occurs successfully. To stabilize charges in the lattice, vacancies of cations are generated .This behavior was justified by Morozov et al. [43] which states that the cationic substitution ($Ca^{2+} \rightarrow Eu^{3+}$) causes the creation of vacancies and that these defects present on the CMO lattice are responsible for the changes recorded in the scheelite type structure. However, it is observed in Fig. 1b that there were no major structural changes. The absence of deleterious phases indicates the purity of the samples. It is observed in the inset of Fig. 2b that the peak associated with the plan (112) showed a shift in the direction of the lower angle to the samples with the highest concentration of Eu^{3+}. The effect of increasing the concentration of Eu^{3+} in CMO lattice is verified by its peak broadening (112) and decrease in its intensity.

The Rietveld refinement method was used to explain possible differences in the structural arrangements induced by the processing of CMO and CMO: xEu particles. This refinement was performed by using the general structure analysis Maud program version 2.0. The results of the Rietveld refinements are shown in Fig. 3. The measured diffraction patterns are well matched to ICSD 60552. The diffractogram corresponding to the experimental and theoretically calculated data are practically identical, as shown in the Obs-Calc line. The results of the refinements are summarized in Table 1. The high quality of the refinements is revealed by the reliability parameters (X^2, *Rwp and Rp*). In addition, the close correspondence between the determined lattice parameters and the unit cell volumes reported in the literature confirms that CMO powders are crystallized in a type of scheelite—tetragonal structure.

The changes in position and intensity of the diffraction peaks occur due to the differences in the sizes of the dopant atoms and cause the repeating distances in the crystal structure to expand or contract depending on the size of the atom that is introduced into the host. In our work, the doping element is the Eu^{3+} that has an ionic radius equal to 1.07 Å smaller than the Ca^{2+} (1.12 Å), forming element of the lattice. It is expected that the lattice parameters of the unit cell presented a decrease in the values; however, this is not perceived according to Table 1. This phenomenon can be perfectly understood due to the rearrangements of the oxygen atoms around the Eu^{3+} in the clusters [EuO_8]. It is observed that with the increase of Eu^{3+} the c/a ratio (tetragonality) decreases. It can be verified that a lattice distortion occurs through a transition from the tetragonal structure to a structure approaching the cubic. This flattening in the c-axis provides small distortions in the structures of [MoO_4] and [CaO_8] clusters distributed within the crystal structure of CMO. As well, these small changes can also be justified by the method of synthesis and experimental conditions (temperature, time, starting precursors) adopted. These variations can lead to several distortions in the Ca–O, Eu–O and/or Mo–O bonds and consequently different levels of distortions in the [CaO_8], [EuO_8] and/or [MoO_4] clusters in the lattice. From the positions of the atoms in the unit cell obtained by the refinement data (see Table 2), it was possible to model the structure of the CMO in each case, using the Vesta program, as shown in Fig. 4. A distortion at the octahedral clusters [$CaO_{8]}$ and/or [EuO_8] clusters is observed withincreased dopant content.

Figure 5 shows that the morfology of the CMO:xEu nanocrystals are still spherical and well defined. It reveals morphology constituted by agglomerates of polycrystalline particles that have a size range between 70 and 251 nm, the largest size values are obtained for the sample treated at 1000 °C. It is observed in Fig. 5a some other dense and hollow particles, this feature is associated to the steps of the method rate of evaporation and precipitation. The high droplet drying rate favors the formation of hollow structures. The surface of the particles has a certain degree of roughness. Figure 5b–d provides images of the doped samples 1, 2 and 4 mol% of Eu^{3+}, it is verified that the particles have distorted shapes. Some of these particles exhibit irregular morphology, associated with the final step in the formation process shown below. It is observed the presence of broken particles with holes. Figure 5 shows the surface of the particle in more details. This image is a characteristic of the cyrstalline morphology.

Raman spectroscopy is an effective tool for studying the effects of structural order and disorder. For a perfect crystal, the first-order Raman phonon spectrum consists of narrow lines that correspond to Raman-allowed zone center-point modes, which obey definite polarization selection rules. In the case of disordered crystals, however, the following features are expected in the phonon spectrum: (i) a broadening of the first-order Raman lines; (ii) activation of forbidden Raman phonons; (iii) appearance of broad Raman bands reflecting the phonon density of states; (iv) frequency shifting of some peaks proportional to the concentration of the dopant element i.e., one-phonon-like behavior; and v splitting of some peaks involving different elements that share the same lattice site i.e., two-phonon-like behavior [44].

According to Basiev et al. [45], the primitive cell of $CaMoO_4$ includes two formulaic units, the MoO_4^{2-} ionic group with strong covalent Mo–O bonds Td symmetry and the Ca^{2+} cations. Due to the weak coupling between the MoO_4^{2-} ionic group and the Ca^{2+} cations, the vibrational modes observed in the spontaneous Raman spectra of $CaMoO_4$ scheelite crystals can be divided into two groups: internal and external modes. The internal vibrons correspond to the vibrations within the MoO_4^{2-}group with

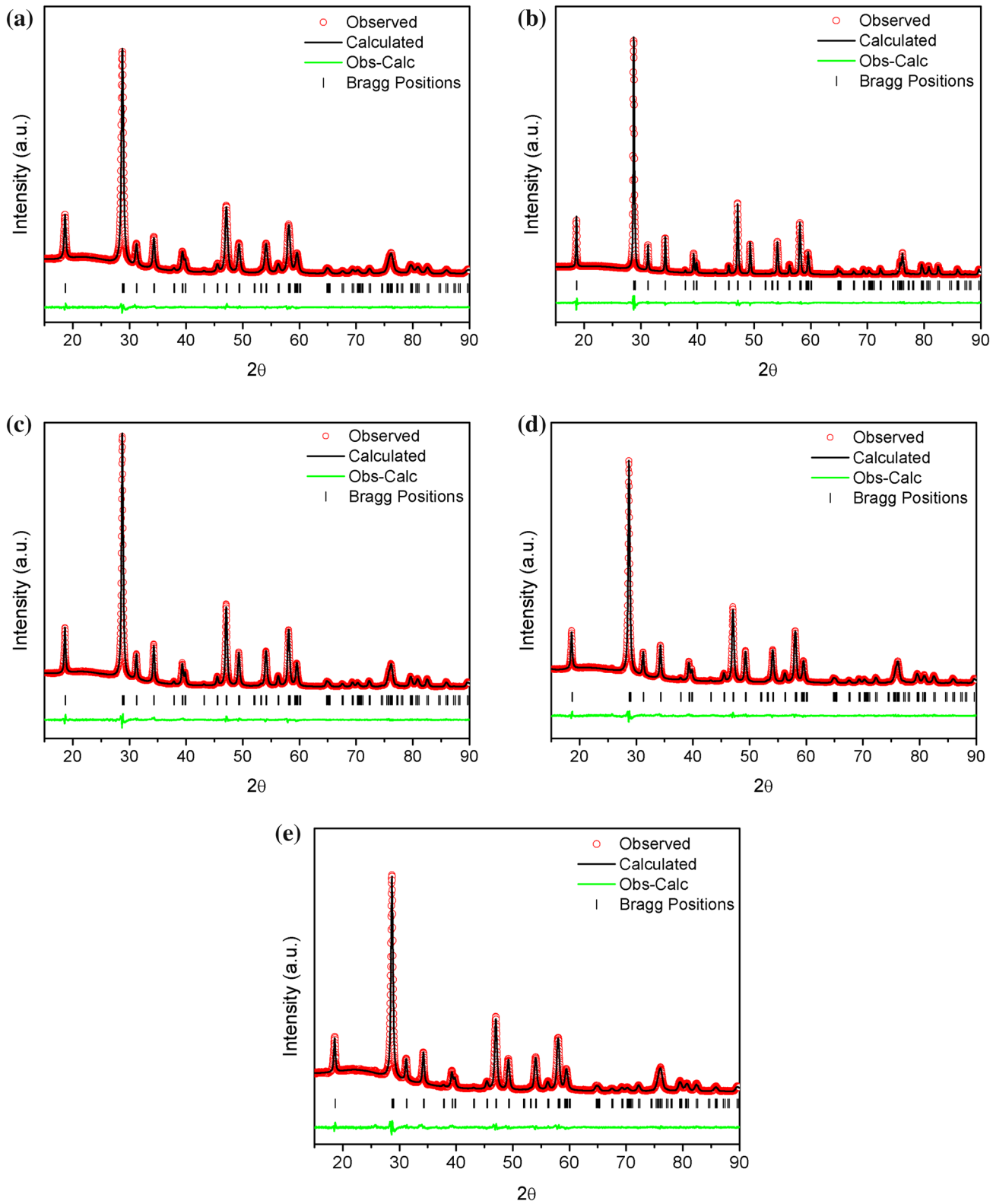

Fig. 3 Rietveld refinements of **a** CMO 600 °C, **b** CMO 1000 °C, **c** CMO: 1% Eu, **d** CMO: 2%, and **e** CMO: 4% Eu nanoparticles

Table 1 Rietveld refined structural parameters for CMO and CMO:xEu^{3+} (1–3 mol%) nanoparticles

Compounds	CMO (600 °C)	CMO (1000 °C)	CMO:1%Eu	CMO:2%Eu	CMO:4%Eu
Crystal system	Tetragonal	Tetragonal	Tetragonal	Tetragonal	Tetragonal
Space group	$I4_1/a$	$I4_1/a$	$I4_1/a$	$I4_1/a$	$I4_1/a$
Lattice parameters (Å)					
a	5.2220	5.2264	5.2237	5.2245	5.2293
c	11.4389	11.4395	11.4386	11.4377	11.4450
c/*a*	2.1905	2.1888	2.1898	2.1892	2.1886
$\alpha=\beta=\gamma$	90°	90°	90°	90°	90°
V $(Å)^3$	311.9319	312.4751	312.1250	312.2003	312.9676
X^2	1.615	1.152	1.871	1.612	1.011
Rwp (%)	2.79	0.68	3.07	0.57	0.33
Rp (%)	2.12	0.39	2.37	0.40	0.21
D (nm)	217.65	391.94	347.37	254.10	229.43
Ɛ $(\times10^{-3})$	2.290	0.177	1.545	1.197	1.937

Table 2 Position of the atoms in the unit cell

Atomic coordinates	CMO (600 °C)	CMO (1000 °C)	CMO:1%Eu	CMO:2%Eu	CMO:4%Eu
Ca/Eu					
x	0.000000	0.000000	0.000000	0.000000	0.000000
y	0.250000	0.250000	0.250000	0.250000	0.250000
z	0.625000	0.625000	0.625000	0.625000	0.625000
Occupancy	1.0000 (Ca)	1.0000 (Ca)	0.9948 (Ca) 0.0100 (Eu)	0.9869 (Ca) 0.0201 (Eu)	1.0028 (Ca) 0.03094 (Eu)
Mo					
x	0.000000	0.000000	0.000000	0.000000	0.000000
y	0.250000	0.250000	0.250000	0.250000	0.250000
z	0.125000	0.125000	0.125000	0.125000	0.125000
Occupancy	1.0000	1.0000	1.0000	1.0000	1.0000
O					
x	0.147595	0.147984	0.146118	0.148796	0.152261
y	0.013268	0.022246	0.014429	0.019030	0.021430
z	0.207617	0.207537	0.208494	0.209415	0.210052
Occupancy	1.0000	1.0000	1.0000	1.0000	1.0000

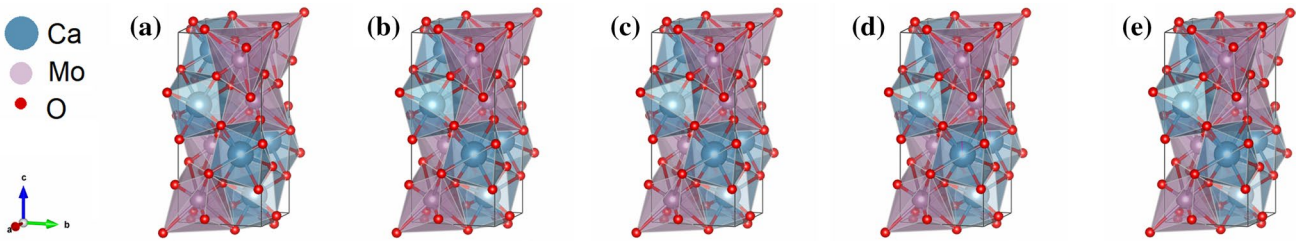

Fig. 4 Model the structure of the **a** CMO 600 °C, **b** CMO 1000 °C, **c** CMO: 1% Eu, **d** CMO: 2%, **e** CMO: 4% Eu nanoparticles

an immovable mass center. The external vibrons or lattice phonons correspond to the motion of the Ca^{2+} cations and the rigid molecular unit. The scheelite primitive cell presents 26 different vibration modes: Td = 3 Ag + 5 Au + 5 Bg + 3 Bu + 5 Eg + 5 Eu, but only Ag, Bg, and Eg are Raman active. The spontaneous Raman spectra with the assignments of the Raman-active vibration modes of

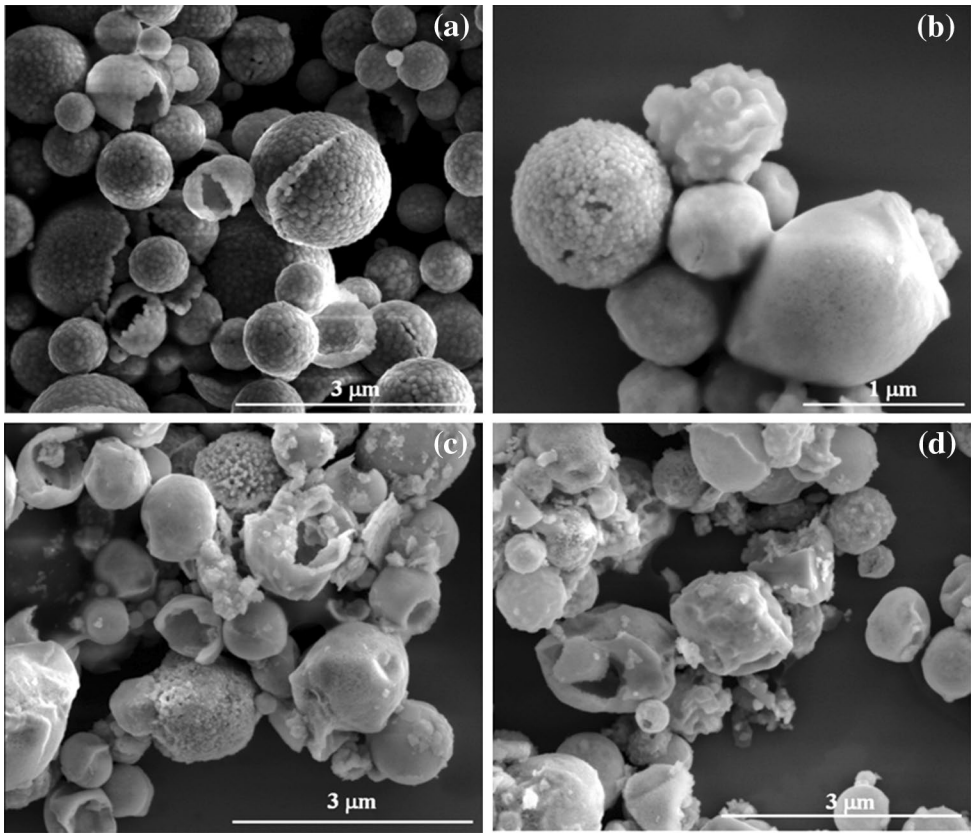

Fig. 5 SEM photos of CMO:xEu—**a** undoped, **b** x: 1 mol% Eu^{3+}, **c** x: 2 mol% Eu^{3+} and **d** x: 4 mol% Eu^{3+}

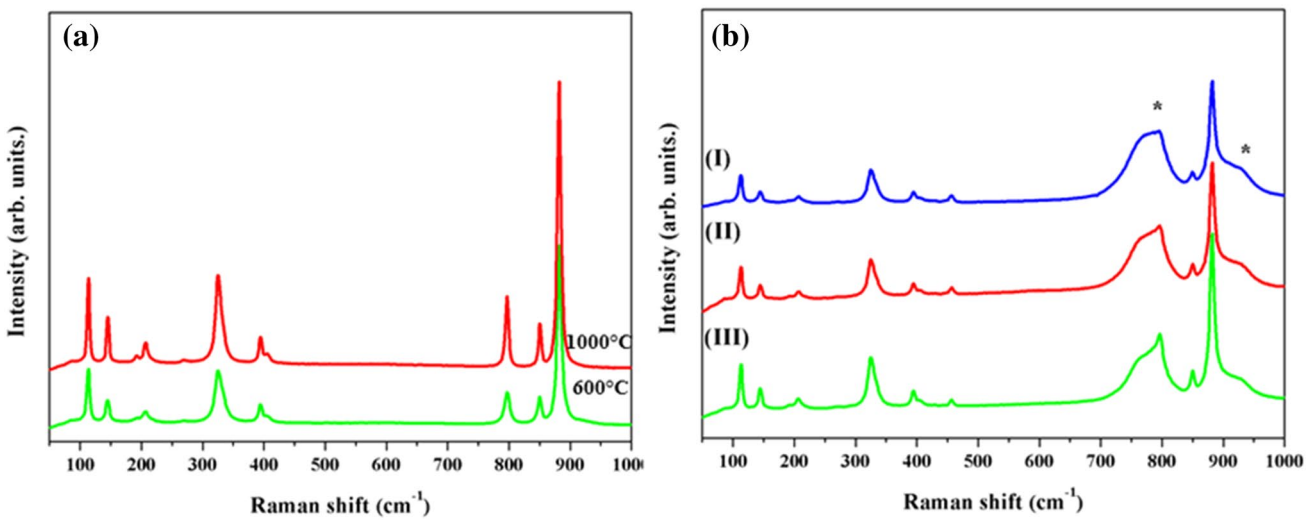

Fig. 6 Raman-active vibration modes of the **a** CMO and **b** CMO:xEu (*I*) x: 1, (*II*) x: 2 and (*III*) x: 4 mol %

the CMO nanopowders are presented in Fig. 6a, b and detailed in Table 3.

The Raman spectra all showed sharp well-resolved peaks external and internal modes for the CMO treated at 600 and 1000 °C, indicating that the synthesized powders were highly crystallized with long- and short-range orders and with few defects such as O vacancies. Vibrational modes characteristic of the scheelite phase in the tetrahedral structure were observed for all samples. They present several peaks referring to the Raman-active internal modes of tetrahedral MoO_4: $\nu 1$ (Ag), $\nu 3$ (Bg), $\nu 3$ (Eg), $\nu 4$ (Eg), $\nu 4$ (Bg), $\nu 2$ (Bg), $\nu 2$ (Ag), R (Ag), R (Eg), and external T (Bg Eg Eg) so they are according to references [46, 47].

Table 3 Raman-active modes results of the CMO and CMO:xEu

Modes	$CaMoO_4$	$CaMoO_4$:Eu	$CaMoO_{4\ valeria}$	$CaMoO_4$:Eu ansari	$CaMoO_{4\ Scott}$
Bg	113	113	112	–	–
Eg	145	144	143	141	–
Ag	192	–	189	191	–
Eg	207	205	205	–	205
Eg	326	326	323	320	318
BgAg	–	–	–	–	333
Bg	395	393	391	389	393
Eg	406	–	402	–	401
Eg	797	795	793	791	797
Bg	851	849	847	843	844
Ag	881	881	878	876	878

It was possible to detect some differences in the Raman spectra of the CMO:xEu samples doped with the specified Eu^{3+} concentrations and the CMO sample heat treated at the same temperature, these differences are presented with (*) in the Fig. 6. Additional fact that proves that the addition of Europium is representative in the samples of this study, is shown by the morphologies of undoped and doped $CaMoO_4$ powders (Fig. 5). When the amount of europium increases, the morphological characteristics of the undoped material are lost, showing that this increase promote the addition of Eu^{+3} is influencing the lattice of the material [48].

The variations found in the Raman spectra marked with (*) demonstrate that with the addition of the dopant, regardless of the percentage used, the materials had an increase of disorder at short-range.

Gonçalves et al., [49] shown in their study, that Raman modes have small shifts which can be caused by distortions in the (O–W–O)/(O–Ca–O) bonds, interaction forces between $[WO_4]$–$[CaO_8]$–$[WO_4]$ clusters and/or different degrees of structural order–disorder in the lattice at short-range, which may be due to the replacement of Ca^{2+} by Eu^{3+} ions. Beside that, other factors may produce different levels of structural order–disorder in the tetragonal lattice such as the preparation method, low temperature of synthesis/processing, geometry and/or crystal size.

We believe that for the $CaMoO_4$: Eu powders synthetized by spray pyrolysis, the distortions cited for tungstates [49] are the same for this study, due to molybdates have the same scheelite structure.

Figure 7 shows the PL spectra of the undoped CMO obtained at different treatment temperatures. The band in the emission spectrum of CMO ranges from 380 to 720 nm, as shown in Fig. 7. There has been a change in the behavior of the emission band due to the effect of the treatment temperature. It can be seen in Fig. 7a that the photoluminescence intensity is abruptly reduced as the treatment temperature increases to 1000 °C. The particles CMO calcined at a lower temperature (600 °C) have lower crystallinity when compared to the CMO particles calcined at 1000 °C. Thus, it is reasonable to consider that materials calcined at lower temperatures show levels of a greater number of present structural defects in the crystal lattice. This degree of order–disorder present in the material structure is recognized as an important factor for the photoluminescent properties. Materials with lower crystallinity index exhibit a significant number of intermediate energy levels in the band gap region. In this condition, electronic transitions occur more easily favoring the photoluminescent emission transitions. It is observed in deconvolute the PL curves shown in Fig. 7b, c a shift of the band towards a lower energy region. It is found that the percentage of the area to the green region decreases from 55 to 45% and there is a growing trend in the percentage of the area to the red region, which parts from 6% to achieve the value of 12%, this behavior is related structural changes occurred in the matrix CMO due to the effect of the heat treatment. There are many explanations in the literature that attempt to justify the origin of the PL properties of $CaMoO_4$. The morphology also influence the PL properties [50], as well as other studies associate PL emission to an appreciable distortion of the tetrahedral clusters $[MoO_4]$ [51]. This symmetry breaking of the cluster may be responsible for the formation of intermediate levels of energy bang gaps [52, 53].

The Photoluminescence phenomenon is reported to be strongly affected by the presence of defects in the lattice such as cation vacancy and vacancy clusters [54] which normally arise during the synthesis or the thermal treatment of the phosphor material.

Many experimental and theoretical studies have been developed in an attempt to justify the appearance of PL properties of CMO [51, 55, 56]. Some strands have been raised as an explanation for the photoluminescent behavior

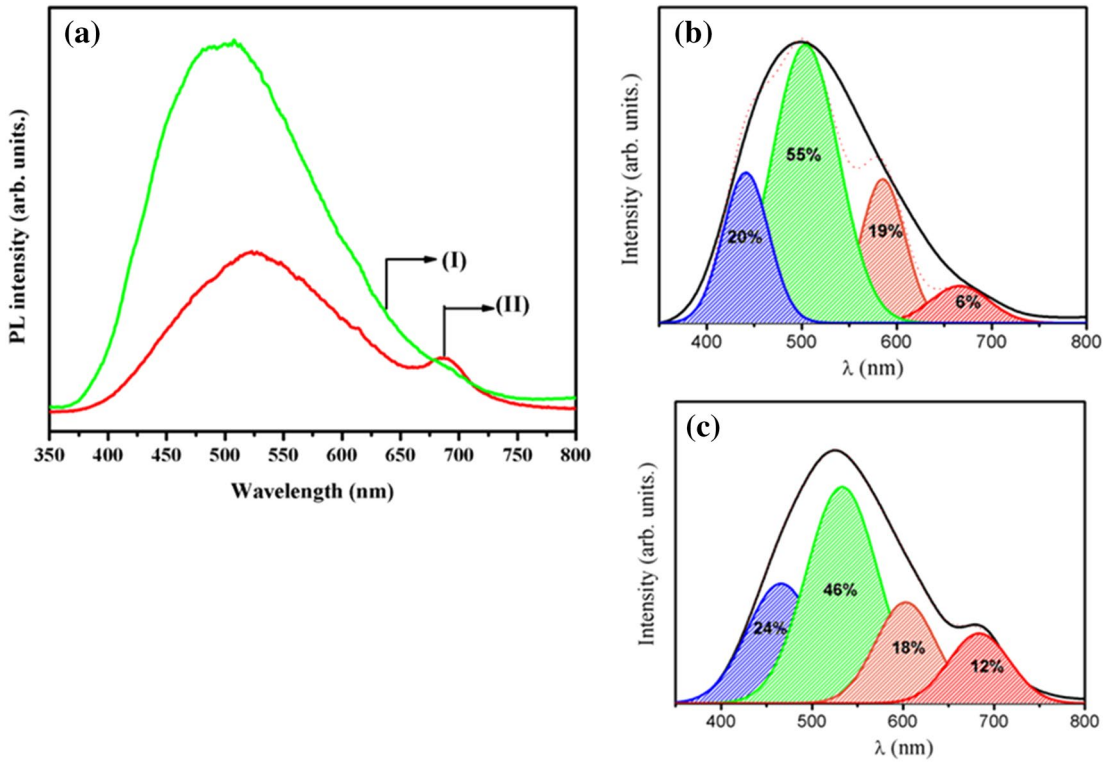

Fig. 7 **a** PL emission spectrum of CMO treated at different temperatures, (*I*) 600 °C and (*II*) 1000 °C; deconvolute the PL *curves*: **b** 600 °C and **c** 1000 °C. (Color figure online)

of the CMO, such as: emissions of energy transfer transitions within the clusters [MoO_4] [57], slight distortions verified in the tetrahedral [MoO_4] [58]. Studies also point out that the particle morphology can also influence photoluminescence (ref) considerably. Stages in the synthesis process such as continuous dissolution and recrystallization during crystalline growth processes can generate defects that induce symmetry breaking in the material, generating the formation of intermediate energy levels within the prohibited bandwidth as discussed above. Gurgel et al. [59] presents a three-stage composite model which proposes to explain the luminescence in the molybdates as illustrated by Fig. 8.

It is shown in Fig. 9a, the PL spectra of the CMO:xEu (x: 1–4 mol%) which were investigated at an excitation wavelength of 350 nm and measured from 350 to 725 nm. The bands shown in Fig. 9 (a) correspond to the state transitions $^5D_0 \rightarrow {}^7F_j$ (j: 0, 1, 2, 3, 4) the setting state of Eu^{3+}, which is located at 581, 594, 615, 660 and 703 nm, respectively. It is known that the transition $^5D_0 \rightarrow {}^7F_2$

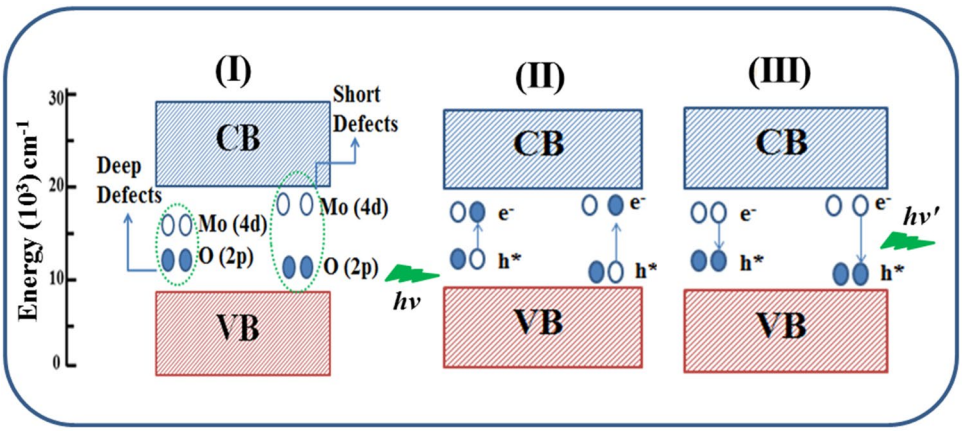

Fig. 8 Model proposed to explain the photoluminescence of CMO. (*I*) The presence of Intermediate levels, represented by short and deep defects within the material gap, is observed. (*II*) Electron transition of oxygen 2*p* orbitals in the valence band (VB) for molybdenum 4*d* orbitals by absorption of (hv) to conduction band (CB). (*III*) Photon emission process (hv′) due to the radiative return of the electrons located in the 4*d* orbitals to the 2*p* orbitals of the oxygen

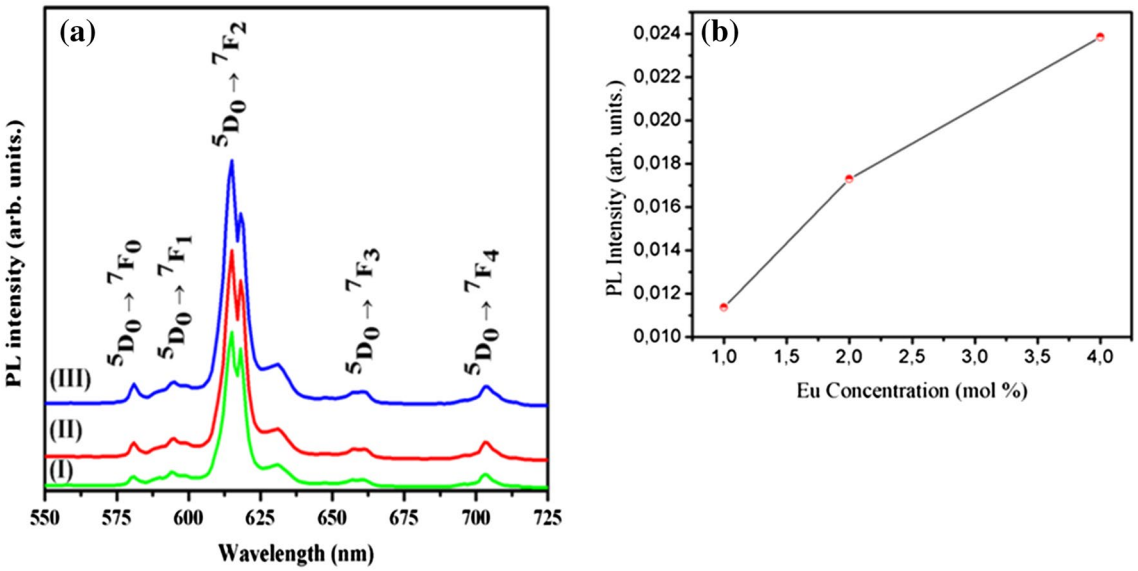

Fig. 9 **a** PL emission spectrum of CMO:xEu (x: 1–4 mol%); **b** variation of PL intensity with Eu^{3+} concentration in $^5D_0 \rightarrow {}^7F_2$ (615 nm)

of Eu^{3+} has a dipole-electric nature, this type of transition is highly sensitive to changes occurring around the Eu^{3+} ion. The transition $^5D_0 \rightarrow {}^7F_1$ has a magnetic dipole nature.

Figure 9b shows the dependence of the red emission $^5D_0 \rightarrow {}^7F_2$ on the Eu^{3+} doping concentration in CMO. It is observed that the increase in the PL intensity is accompanied by an increase in the concentration of Eu^{3+}. The PL intensity maximum corresponds to the sample doped with 4 mol% of Eu^{3+}.

Figure 10 shows the CIE coordinates of CMO and CMO:xEu, while Table 4 lists the CIE coordinate values and CCT values for samples. The CIE coordinates are obtained from spectral distributions that allow us to define three tristimulus values X, Y and Z. Based on these values you can set the chromaticity of a certain color from only two coordinates (x' y'). The CCT value was estimated by using McCamy empirical formula [60]. The quality of white light is calculated using McCamy empirical equation (2) in terms of CCT values, which is expressed as:

$$CCT = -449n^3 + 3525n^2 - 6823n + 5520.33 \quad (2)$$

where $n = \frac{(x'-xe)}{(y'-ye)}$ is the inverse slope line, $xe = 0.332$ and $ye = 0.186$.

We obtained white light emission from particles of CMO thermally treated 1000 °C. It is noticed that the wide band PL emission (Fig. 7) has the contribution of the blue green and red regions of the electromagnetic spectrum. This precise cooperation of each region of the visible spectrum was satisfactory to obtain the material with white light emission. The samples doped with Eu^{3+} showed emission in the orange region, this result is consistent with previous studies [61], the transition more intense emission located at 615 nm corresponding to orange band—red in the visible spectrum.

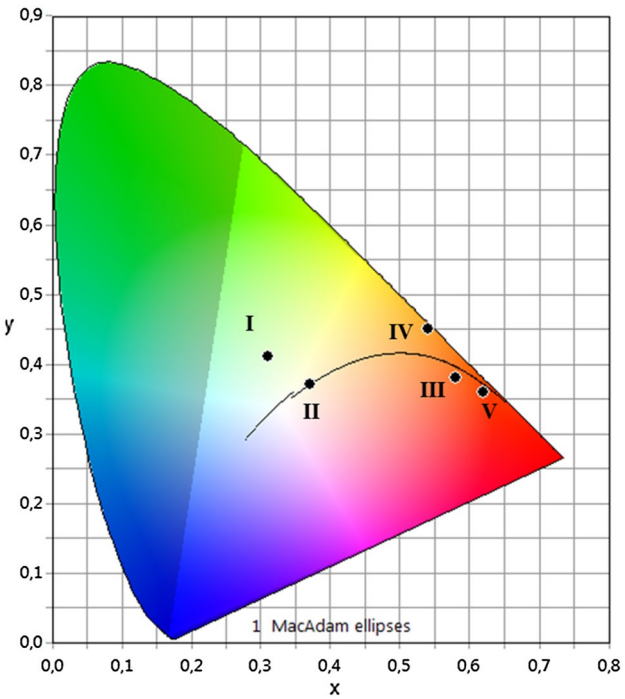

Fig. 10 CIE chromaticity diagram of of CMO and CMO:xEu

Table 4 Chromaticity coordinates (CIE) and correlated temperature color (CCT) for CMO and CMO:xEu

Code	Samples	CIE (x', y')	CCT (K)	Color
I	CMO (600 °C)	(0.31, 0.41)	6218	Yellowish green
II	CMO (1000 °C)	(0.37, 0.37)	4251	White
III	CMO: 1% Eu	(0.58, 0.38)	1466	Orange
IV	CMO: 2% Eu	(0.54, 0.45)	2112	Yellowish orange
V	CMO: 4% Eu	(0.62, 0.36)	1189	Reddish orange

4 Conclusion

The particles of CMO and CMO:xEu were obtained successfully by the spray pyrolysis method. According to XRD results, the identified phase was tetragonal, free of secondary phases. The particles are spherical and present a well defined morphology. Some particles exhibited an irregular shape with some distortion, this aspect is involved in the final step of the process to obtain the material. By Raman spectroscopy it was possible to recognize the internal vibrational modes related the Mo–O bonds and external vibrational modes related to phonons due to the movement of Ca^{2+} cations. It is inferred a different behavior for samples doped with Eu^{3+} by the presence of bands around 800 and 950 cm^{-1} and confirmed the presence of Eu^{3+} in the CMO structure. The PL emission spectra for CMO particles had a broadband behavior. According to the spectral distribution, CIE coordinates calculated (0.37, 0.37) to 1000 °C exhibited emission of white light by specific contributions in the **B** (blue), **G** (green) and **R** (red) regions. The PL results for samples doped with Eu^{3+}showed emissions in the red–orange. The intensity of the luminescence increases with the concentration of Eu^{3+} ion.

References

1. C. Hazra, T. Samanta, A.V. Asaithambi, V. Mahalingam, Dalton Trans. **43**, 6623 (2014)
2. G.S.R. Raju, E. Pavitra, Y.H. Ko, J.S. Yu, J. Mater. Chem. **22**, 15562 (2012)
3. S.P. Culver, F.A. Rabuffetti, S. Zhou, M. Mecklenburg, Y. Song, B.C. Melot, R.L. Brutchey, Chem. Mater. **25**, 4129 (2013)
4. A.K. Parchur, R.S. Ningthoujam, Dalton Trans. **40**, 7590 (2011)
5. E. Cavalli, P. Boutinaud, R. Mahiou, M. Bettinelli, P. Dorenbos, **49**, 4916 (2010)
6. A.K. Parchur, A.I. Prasad, A.A. Ansari, S.B. Rai, R.S. Ningthoujam, Dalton Trans. **41**, 11032 (2012)
7. Y. Yang, X. Li, W. Feng, W. Yang, W. Li, C. Tao, J. Alloys Compd. **509**, 845 (2011)
8. Y. Jin, J. Zhang, Z. Hao, X. Zhang, X.-j. Wang J. Alloys Compd. **509**, L348 (2011)
9. J.H. Chung, S.Y. Lee, K.B. Shim, S.-Y. Kweon, S.-C. Ur, J.H. Ryu, Appl. Phys. A **108**, 369 (2012)
10. A.V. Veresnikova, B.K. Lubsandorzhiev, I.R. Barabanov, P. Grabmayr, D. Greiner, J. Jochum, M. Knapp, C. Oßwald, R.V. Poleshuk, F. Ritter, B.A.M. Shaibonov, Y.E. Vyatchin, G. Meierhofer, Nucl. Instrum. Methods Phys. Res. Sect. A **603**, 529 (2009).
11. J.H. Ryu, J.-W. Yoon, C.S. Lim, W.-C. Oh, K.B. Shim, J. Alloys Compd. **390**, 245 (2005)
12. C. Cui, J. Bi, D. Gao, Appl. Surf. Sci. **255**, 3463 (2008)
13. V.B. Mikhailik, H. Kraus, Phys. Status Solidi (B), **247** 1583 (2010).
14. S. Dutta, S. Som, S.K. Sharma, Dalton Trans. **42**, 9654 (2013)
15. B.P. Singh, A.K. Parchur, R.S. Ningthoujam, A.A. Ansari, P. Singh, S.B. Rai, Dalton Trans. **43**, 4779 (2014)
16. E. Gürmen, E. Daniels, J.S. King, J. Chem. Phys. **55**, 1093 (1971)
17. S.H. Yu, B. Liu, M.S. Mo, J.H. Huang, X.M. Liu, Y.T. Qian, Adv. Funct. Mater. **13**, 639 (2003)
18. Y.-S. Luo, W.-D. Zhang, X.-J. Dai, Y. Yang, S.-Y. Fu, J. Phys. Chem. C **113**, 4856 (2009)
19. J. Liu, X. Huang, Y. Li, Z. Li, J. Mater. Chem. **17**, 2754 (2007)
20. Q. Gong, X. Qian, X. Ma, Z. Zhu, Cryst. Growth Des. **6**, 1821 (2006)
21. N. Sharma, K.M. Shaju, G.V. Subba Rao, B.V.R. Chowdari, Z.L. Dong, T.J. White, Chem. Mater. **16**, 504 (2004)
22. C. Xu, D. Zou, H. Guo, F. Jie, T. Ying, J. Lumin. **129**, 474 (2009)
23. T. Thongtem, S. Kungwankunakorn, B. Kuntalue, A. Phuruangrat, S. Thongtem, J. Alloys Compd. **506**, 475 (2010)
24. Y. Sun, J. Ma, X. Jiang, J. Fang, Z. Song, C. Gao, Z. Liu, Solid State Sci. **12**, 1283 (2010)
25. T. Titipun, P. Anukorn, T. Somchai, J. Ceram Process. Res. **9**, 189 (2008)
26. J.H. Ryu, S.Y. Bang, J.-W. Yoon, C.S. Lim, K.B. Shim, Appl. Surf. Sci. **253**, 8408 (2007)
27. Z. Hou, R. Chai, M. Zhang, C. Zhang, P. Chong, Z. Xu, G. Li, J. Lin, Langmuir **25**, 12340 (2009)
28. Y. Zhou, J. Liu, X. Yang, X. Yu, L. Wang, J. Electrochem. Soc. **158**, K74 (2011)
29. W. Wang, Y. Hu, J. Goebl, Z. Lu, L. Zhen, Y. Yin, J. Phys. Chem. C **113**, 16414 (2009)
30. J. Brübach, T. Kissel, M. Frotscher, M. Euler, B. Albert, A. Dreizler, J. Lumin. **131**, 559 (2011)
31. S.S. Hosseinpour-Mashkani, S.S. Hosseinpour-Mashkani, A. Sobhani-Nasab, J. Mater. Sci. **27**, 4351 (2016)
32. I. Taniguchi, Mater. Chem. Phys. **92**, 172 (2005)
33. G. Biskos, V. Vons, C. U. Yurteri, A. Schmidt-Ott, Kona Powder Part. J. **26**, (2008)
34. Y.C. Kang, S.B. Park, J. Mater.Sci. **31**, 2409 (1996)
35. A. Dalmoro, A.A. Barba, M. D'Amore, Sci. World J. **482910**, 1 (2013)
36. A.K. Parchur, R.S. Ningthoujam, S.B. Rai, G.S. Okram, R.A. Singh, M. Tyagi, S.C. Gadkari, R. Tewari, R.K. Vatsa, Dalton Trans. **40**, 7595 (2011)
37. Y. Hu, W. Zhuang, H. Ye, D. Wang, S. Zhang, X. Huang, J. Alloys Compd. **390**, 226 (2005)
38. J. Liu, H. Lian, C. Shi, Opt. Mater. **29**, 1591 (2007)
39. A.A. Ansari, A.K. Parchur, M. Alam, A. Azzeer, Spectrochim. Acta Part A **131**, 30 (2014)
40. X.-F. Wang, G.-H. Peng, N. Li, Z.-H. Liang, X. Wang, J.-L. Wu, J. Alloys Compd. **599**, 102 (2014)
41. S. Mahlik, M. Behrendt, M. Grinberg, E. Cavalli, M. Bettinelli, J. Phys. Condens. Matter **25**, 105502 (2013)
42. F. Brunetti, *Mechanics of Fluids*, 2ª Ed, (Pearson, São Paulo, 2008)

43. V.A. Morozov, B.I. Lazoryak, S.Z. Shmurak, A.P. Kiselev, O.I. Lebedev, N. Gauquelin, J. Verbeeck, J. Hadermann, G. Van Tendeloo, Chem. Mater. **26**, 3238 (2014)
44. M. Moura, A. Ayala, I. Guedes, M. Grimsditch, C. Loong, L. Boatner, J. Appl. Phys. **95**, 1148 (2004)
45. T. Basiev, A. Sobol, Y.K. Voronko, P. Zverev, Opt. Mater. **15**, 205 (2000)
46. V.M. Longo, A.T. Figueiredo, A.B. Campos, J.W. Espinosa, A.C. Hernandes, C.A. Taft, J.R. Sambrano, J.A. Varela, E. Longo, J. Phys. Chem. A **112**, 8920 (2008)
47. A. Phuruangrat, T. Thongtem, S. Thongtem, J. Alloys Compd. **481**, 568 (2009)
48. F.V. Motta, A.P.A. Marques, M.S. Li, M.F.C. Abreu, C.A. Paskocimas, M.R.D. Bomio, R.P. Souza, J.A. Varela, E. Longo, J. Alloys Compd. **553**, 338 (2013)
49. R.F. Gonçalves, L.S. Cavalcante, I.C. Nogueira, E. Longo, M.J. Godinho, J.C. Sczancoski, V.R. Mastelaro, I.M. Pinatti, I.L.V. Rosa, A.P.A. Marques. CrystEngComm. **17**, 1654 (2015)
50. J.H. Ryu, J.W. Yoon, C.S. Lim, W.C. Oh, K.B. Shim, J. Alloy. Compd. **390**, 245 (2005)
51. V.M. Longo, A.T. de Figueiredo, A.B. Campos, J.W.M. Espinosa, A.C. Hernandes, C.A. Taft, J.R. Sambrano, J.A. Varela, E. Longo, J. Phys. Chem. A **112**, 8920 (2008)
52. M.R.D. Bomio, L.S. Cavalcante, M.A.P. Almeida, R.L. Tranquilin, N.C. Batista, P.S. Pizani, M.S. Li, J. Andres, E. Longo, Polyhedron **50**, 532 (2013)
53. J.C. Sczancoski, M.D.R. Bomio, L.S. Cavalcante, M.R. Joya, P.S. Pizani, J.A. Varela, E. Longo, M.S. Li, J.A. Andres, J. Phys. Chem. C **113**, 5812 (2009)
54. T. Selvalakshmi, S. Sellaiyan, A. Uedono, A.C. Bose, Investigation of defect related photoluminescence property of multicolour emitting Gd_2O_3:Dy^{3+} phosphor. RSC Adv. **4**, 34257 (2014)
55. T. Thongtem, S. Kungwankunakorn, B. Kuntalue, A. Phuruangrat, S. Thongtem, J. Alloy Compd. **506**, 475 (2010)
57. V.M. Longo, L.S. Cavalcante, E.C. Paris, J.C. Sczancoski, P.S. Pizani, M.S. Li, J. Andres, E. Longo, J.A. Varela, J. Phys. Chem. C **115**, 5207 (2011)
57. A. Phuruangrat, T. Thongtem, S. Thongtem, J. Alloy. Compd. **481**, 568 (2009)
58. Y. Xiang, J. Song, G. Hu, Y. Liu, Appl. Surf. Sci. **349**, 374 (2015)
59. G.M. Gurgel, L.X. Lovisa, O.L.A. Conceicão, M.S. Li, E. Longo, C.A. Paskocimas, F.V. Motta, M.R. Bomio, J. Mater. Sci. **52**, 4608 (2017)
60. C.S. McCamy. Correlated color temperature as an explicit function of chromaticity coordinates, Color Res. Appl. (1992). doi:10.1002/col.5080170211
61. J. Choi, T.-K. Tseng, M. Davidsonab, P. H. Hollowaya, Enhanced photoluminescence from Gd_2O_3:Eu^{3+} nanocores with a Y_2O_3 thin shell, J. Mater. Chem. **21**, (2011) 3113